Aeroacoustics Conferences
26-29 May 2026, Brussels, Belgium
32nd AIAA/CEAS Aeroacoustics Conference (2026)

10.2514/6.2026-3207

Check for updates

PIV analysis of noise generation mechanisms in the leading-edge slat cavity using POD and cross-correlation

Fernando de Paula*†
Federal University of Santa Catarina (UFSC), Joinville, Brazil
Ecole Centrale de Lyon, CNRS, Universite Claude Bernard Lyon 1, INSA Lyon, LMFA, UMR5509, 69130, Ecully, France.

Antonio Pereira‡, Emmanuel Jondeau§, Marc C. Jacob¶
Ecole Centrale de Lyon, CNRS, Université Claude Bernard Lyon 1, INSA Lyon, LMFA, UMR5509, 69130 Écully, France

Filipe Dutra da Silva‖
Federal University of Santa Catarina (UFSC), Joinville, Brazil

With the exponential growth of the global aircraft fleet, airport communities have become more susceptible to exposure to noise emitted in their surroundings, which can lead to serious health problems for the population. Significant advances have been made in reducing aircraft engine noise in recent decades, while so-called airframe noise has become one of the main sources of noise pollution, particularly the noise generated by slats during landing. In this context, this paper presents an experimental analysis of the noise generated by a wing element equipped with a slat in the anechoic wind tunnel of the Fluid Mechanics and Acoustics Laboratory at École Centrale de Lyon at different speeds. Several acquisition techniques, such as Particle Image Velocimetry (PIV), an array of far-field directivity microphones and phased array microphones, were employed to identify the main aerodynamic phenomena responsible for noise radiation. In addition, advanced post-processing techniques such as Proper Orthogonal Decomposition (POD), Spectral POD and cross-correlation analysis were employed to extract dominant flow structures, identify characteristic frequency components, and quantify spatial and temporal relationships within the data.

I. Nomenclature

a_i	=	time coefficient of Mode i
c	=	deployed wing chord
f	=	frequency
f_s	=	PIV sampling frequency
k_{high}	=	cutoff mode for highly correlated POD modes
k_{mod}	=	cutoff mode for moderately correlated POD modes
N	=	number of points inside investigation window
R	=	cross-correlation coefficient
Re_c	=	chord-based Reynolds number
s	=	slat chord
St	=	Strouhal number
U	=	horizontal component of velocity
u'	=	fluctuations of u
U_∞	=	free-stream velocity

*Undergraduate Student, Thermofluids Engineering Group (TEG), Federal University of Santa Catarina (UFSC), Joinville, Brazil.
†Master's Student, Laboratoire de Mécanique des Fluides et d'Acoustique (LMFA), École Centrale de Lyon, Ecully, France.
‡Research Engineer, LMFA – École Centrale de Lyon, Écully, France.
§Research Engineer, LMFA – École Centrale de Lyon, Écully, France.
¶Professor, LMFA – École Centrale de Lyon, Écully, France.
‖Assistant Professor, Thermofluids Engineering Group (TEG), Federal University of Santa Catarina (UFSC), Joinville, Brazil.

V	=	vertical component of velocity
$\|\mathbf{V}\|$	=	magnitude of velocity
Γ_1,Γ_2	=	vortex identification probability functions
θ_M	=	angle between $\overline{PM}$ and $\mathbf{U_M}$
ω	=	vorticity

II. Introduction

Concerns regarding aircraft noise gained prominence during the 1960s, driven by increasing air traffic and the growing demand for more powerful aircraft and engines. Communities residing near airports began to report significant discomfort due to noise pollution, which has been associated with adverse effects such as hearing loss, reduced task performance, impaired speech intelligibility, sleep disturbances, and general annoyance [1].

In light of this issue, reducing the number of individuals exposed to aircraft noise has become a priority for the International Civil Aviation Organization (ICAO) [2], which, in 2014, introduced Chapter 14 to Annex 16. This amendment resulted in a 7 dB reduction in the Effective Perceived Noise Level (EPNdB) compared to previous limits. According to ICAO [2], it is estimated that by 2036 more than one million people will be relocated from areas exposed to noise levels exceeding 55 dB. In addition to the health benefits, aircraft noise reduction can also yield significant economic advantages, as a decrease of only 1 dB in cumulative daily noise levels may enable up to a 20% increase in aircraft fleet operations [3].

In commercial aviation—particularly during landing phases—noise generated by slats remains a major concern. This is due to the fact that a wing, in its clean cruise configuration, is not capable of providing sufficient lift throughout all flight phases. Consequently, high-lift devices are essential. The slat, specifically, enhances the maximum lift coefficient performance ($C_{l_{max}}$) across a range of angles of attack (AoA), as demonstrated by Anderson [4].

With the advent of high-bypass turbofan engines, which are quieter compared to traditional jet engines, airframe noise has become one of the major sources of aircraft noise pollution [5]. As highlighted by Zhang et al. [6], based on a comprehensive literature review, airframe noise during the approach phase is significantly higher than during takeoff. Among the various noise sources present during landing, slats have been identified as the primary contributors to environmental noise pollution.

In this context, understanding the noise dynamics generated by high-lift devices—such as slats and flaps—becomes essential. Unlike other noise sources, progress in mitigating noise from these devices remains limited. Initial studies have identified that slat noise is primarily dominated by flow instability mechanisms, particularly in the slat cavity region [7–9]. These investigations employed techniques such as wind tunnel measurements and computational simulations to explore the underlying noise generation mechanisms.

The flow behavior within the slat cavity has been further analyzed using techniques such as Particle Image Velocimetry (PIV), wall-pressure measurements, and beamforming. These analyses have revealed a direct correlation between coherent flow structures—such as Kelvin–Helmholtz vortices—and the observed noise emission patterns. Moreover, Pascioni and Cattafesta [10] demonstrated the influence of the angle of attack on both the location and intensity of acoustic sources, reinforcing the role of the slat as the dominant noise source in high-lift configurations.

Terracol et al. [11] investigated the noise generation mechanisms in the slat cove region using zonal hybrid Reynolds-averaged Navier Stokes - large eddy simulation (RANS/LES), aiming to accurately describe the internal flow dynamics of the slat cavity and the processes responsible for sound emission. From these simulations, the authors performed a detailed analysis of the coherent structures formed within the cavity, identifying instabilities that lead to tonal noise emission. The numerical results were compared with available experimental data, enabling validation of the predictions and reinforcing the relevance of the adopted approach. Despite the quality of the results, the authors emphasize the need for further studies to deepen the correlation between flow structures and acoustic sources.

Henning et al. [12] conducted an experiment aimed at investigating the relationship between flow structures in the slat cove region and the radiated noise. To achieve this, they combined synchronized PIV measurements with microphones, applying cross-correlation techniques. Through this approach, the authors identified that coherent structures generated in the shear layer of the flow within the slat cavity exhibited a strong association with the tonal peaks observed in the noise spectrum. This reinforces the hypothesis that these structures are responsible for the dominant noise generation mechanisms in high-lift configurations.

Mironov et al. [13] analyzed the impact of using serrated trailing edges applied to the slat as a method of noise reduction. Their results demonstrated that this geometric modification can lead to a significant attenuation of narrowband noise components, particularly at moderate angles of attack. This reduction was attributed to the disruption of coherent flow structures responsible for tonal noise generation.

Given this context, the present work focuses on experimentally characterizing the flow mechanisms responsible for slat-cavity noise and examining their relation to the radiated acoustic field. The study combines time-resolved PIV, wall-pressure measurements, and far-field and phased-array acoustic data acquired in the anechoic wind tunnel of the Laboratoire de Mécanique des Fluides et d'Acoustique (LMFA). Post-processing tools such as Proper Orthogonal Decomposition, vortex-identification methods, and velocity–pressure cross-correlation are employed to link coherent flow structures with the dominant noise-generation mechanisms. This integrated approach builds upon previous efforts [10, 12], with a similar focus on identifying the dominant noise-generation mechanisms.

III. Methodology

A. Wind tunnnel facility

Experiments were conducted in LMFA's anechoic wind-tunnel facility at École Centrale de Lyon, which couples silent sub- and supersonic air-supply lines to a 10 m × 8 m × 8 m anechoic chamber. A two-stage 800 kW centrifugal fan delivers flow speeds up to Mach 0.8 for the subsonic configuration through silenced ducts, so background noise is kept to a minimum.

The wind-tunnel exit duct has a square cross-section with 0.56 m sides. For this experiment, a convergent nozzle was used, reducing the flow to a rectangular section measuring 0.50 m in width and 0.40 m in height. Also, to suppress unwanted noise at low frequencies, brush seals were mounted along the downstream edges of the end plates. The setup is shown in Fig. 1. This unique university-scale rig provides the free-field acoustic conditions and high-quality flow necessary for aeroacoustic studies of most aeronautical devices.

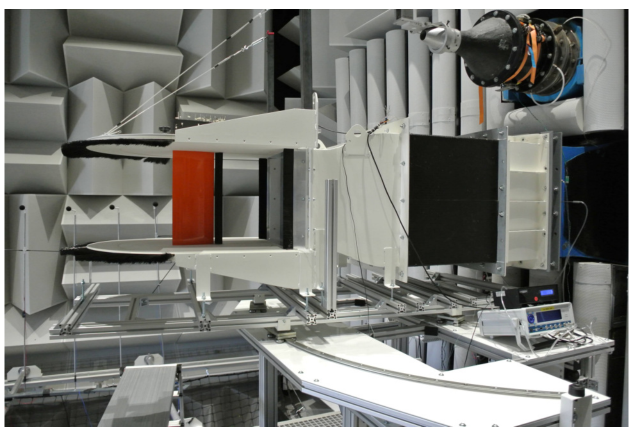

Fig. 1 Picture of the experimental setup showing the convergent nozzle, the airfoil and the slat in orange and black colors respectively. Some of directivity microphones are seen in the back.

B. Airfoil geometry

Experiments were carried out on an adapted German Aerospace Center (DLR) F16, originally a 3-element airfoil, consisting of a leading-edge slat and a main wing, DLR has used this airfoil extensively, building multiple geometrically similar models at various scales [14]. Fig. 2 shows a schematic of the 2D model, which has a stowed chord of c = 0.200 m and a span of 0.400 m; the slat chord is $s = 0.186\ c = 0.0372$ m and is set at a deflection angle of 28.814°. More details about the geometry can be found in reference [11]. The assembly is mounted between upper and lower plates with turntables, where both the slat and main wing are fixed, eliminating the need for slat tracks.

Measurements were performed at three different free-stream velocities: $U_\infty = 25\,\mathrm{m\,s^{-1}}$ ($Re_c = 3.38 \times 10^5$), $50\,\mathrm{m\,s^{-1}}$ ($Re_c = 6.77 \times 10^5$), and $75\,\mathrm{m\,s^{-1}}$ ($Re_c = 1.01 \times 10^6$), where c was used as the characteristic length in the definition of the Reynolds number.

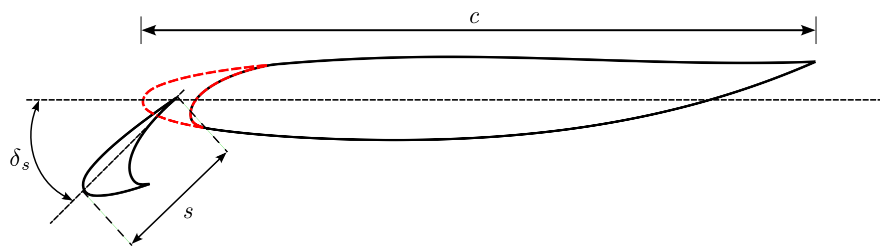

Fig. 2 Two-element airfoil used in the study. The dashed red line represents the stowed configuration

C. Acoustic acquisition

For the acoustic measurements, a circular array of seven GRAS 46BE 1/4" microphones, each with a sensitivity of approximately $3.6\,\mathrm{mV\,Pa^{-1}}$ and a frequency response ranging from 4 Hz to 80 kHz, was mounted alongside the flow, as depicted in Fig. 3a. On both the extrados and intrados sides, the array was positioned so that its central microphone (M4, at 90° relative to the flow direction) lay on the slat's trailing-edge line at an approximate distance of 2 m, while the remaining microphones were spaced at 10° increments. Because the laser sheet had to impinge on the wing at normal incidence, PIV and acoustic measurements could not be taken on the same side of the flow simultaneously. Fig. 3a shows the PIV acquisition on the model's intrados, while acoustic data were recorded on its extrados; the setup was then reversed for subsequent runs. Each run lasted 0.98 seconds: ten runs were recorded at $U_\infty = 50\,\mathrm{m\,s^{-1}}$ and five runs for $U_\infty = 25\,\mathrm{m\,s^{-1}}$ and $U_\infty = 75\,\mathrm{m\,s^{-1}}$. A scheme for the setup is presented in Fig. 3a.

Besides the microphone array, an LMS Sound Camera Digital Array (phased microphone array) was used to localize noise sources and visualize their spatial distribution across the element surface using beamforming techniques. The array consisted of 117 MEMS (Micro-Electro-Mechanical Systems) sensors arranged in spiral configurations across 9 radial branches as shown in Fig. 3b.

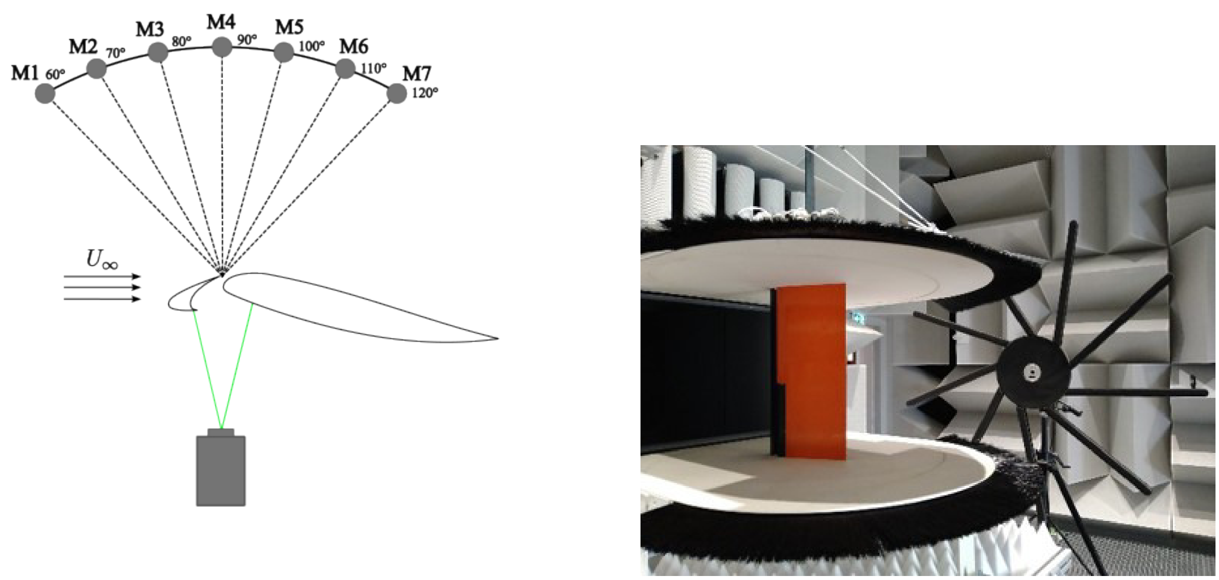

(a) Directivity microphones and PIV setup together

(b) Phased microphone array

Fig. 3 Experimental acoustic measurement setups

D. Wall pressure measurements

The wing and slat include thin internal channels that allow wall-pressure measurements. Steady pressures were recorded with a Kulite KMPS-1-64-XX-Y Series pressure scanner, featuring a pressure range up to 1 PSI (6864 Pa) with an accuracy of 0.12 % of that value. Unsteady pressure fluctuations were captured by Brüel & Kjær 1/4" Type 4958 microphones mounted using a remote probe configuration, with a sensitivity of 11.2 mV Pa^{-1}, a frequency range of 10 –20 000 Hz, and a dynamic range of 28 –140 dB. For the unsteady wall-pressure signals, a frequency-response function (FRF) was measured to correct the attenuation and phase lag introduced by the remote access. The technique for measuring the calibration FRFs is detailed in [15]. Fig. 4 illustrates the locations of the wall-pressure acquisition probes on the airfoil.

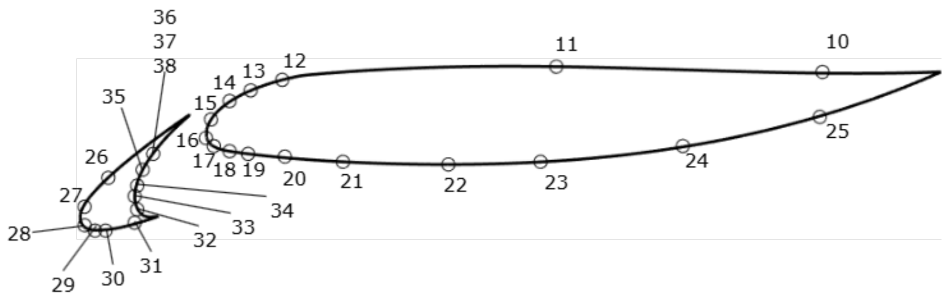

Fig. 4 Locations of the pressure probes on the wing element

E. PIV Setup

Particle Image Velocimetry (PIV) is a widely used flow visualization technique in aerodynamics. There are several variants depending on the experimental setup, such as 2D PIV, Tomographic PIV (Tomo-PIV), Time-Resolved PIV (TR-PIV), and Stereo PIV. In this campaign, two-dimensional time-resolved PIV (2D TR-PIV) was performed at mid-span of the airfoil. The system configuration is shown in Fig. 5a, which depicts the articulated arm used to guide the PIV laser beam up to the slat cavity. The camera is placed underneath the lower side plate and views the slat cavity through an optical aperture. This section focuses on describing the general methodology.

The flow was seeded using Feuerwehr Extra SAFEX Inside Nebelfluid particles, with an average diameter of approximately 1 nm. These particles were injected at the compressor inlet, well upstream of the test section, allowing them to disperse homogeneously throughout the flow. Particle sizing using Phase Doppler Anemometry (PDA) revealed a size distribution ranging from 0.514 nm (lower limit set by the green laser wavelength) to 3 nm. This ensured that the particles followed the flow effectively and were evenly distributed.

Illumination was provided by a Mesa PIV 532-120-M dual-pulse laser (Amplitude Laser®), emitting at 532 nm with 9 mJ per pulse. The laser beam was directed through an articulated arm. Velocity-field measurements were captured over a field of view of 166.8 mm × 222 mm, with a spatial resolution of 5.76 px mm^{-1}. Data acquisition and processing were carried out using Davis 10.1.2 software (LaVision).

The time-resolved PIV (TR-PIV) was sampled at $f_s = 5$ kHz, with an acquisition time of 0.98 s, yielding 4900 images per run. A trigger system was set up to ensure that all images were recorded within the same time interval as the acoustic measurements, allowing for precise synchronization between the PIV and acoustic data. Velocity vectors were computed using a multi-pass cross-correlation algorithm with a final interrogation window of 12 px × 12 px and 50% overlap. Post-processing included peak ratio and residual threshold filters to eliminate spurious vectors. For more details on the algorithm and its parameters, refer to [16].

Four distinct regions of interest were targeted in the PIV measurements: the slat cove, the area after the slat trailing edge, the full extrados of the main element, and its intrados. The schematic for this configuration is shown in Fig. 5b.

IV. Results

This section presents the post-processed PIV and acoustic data, including velocity fields for the entire wing and detailed views of the key regions of interest, particularly the slat cove and its exit toward the wing's extrados. Additionally, Proper Orthogonal Decomposition (POD) was applied to the PIV velocity fields to extract the dominant energetic modes and shed light on the underlying flow phenomena.

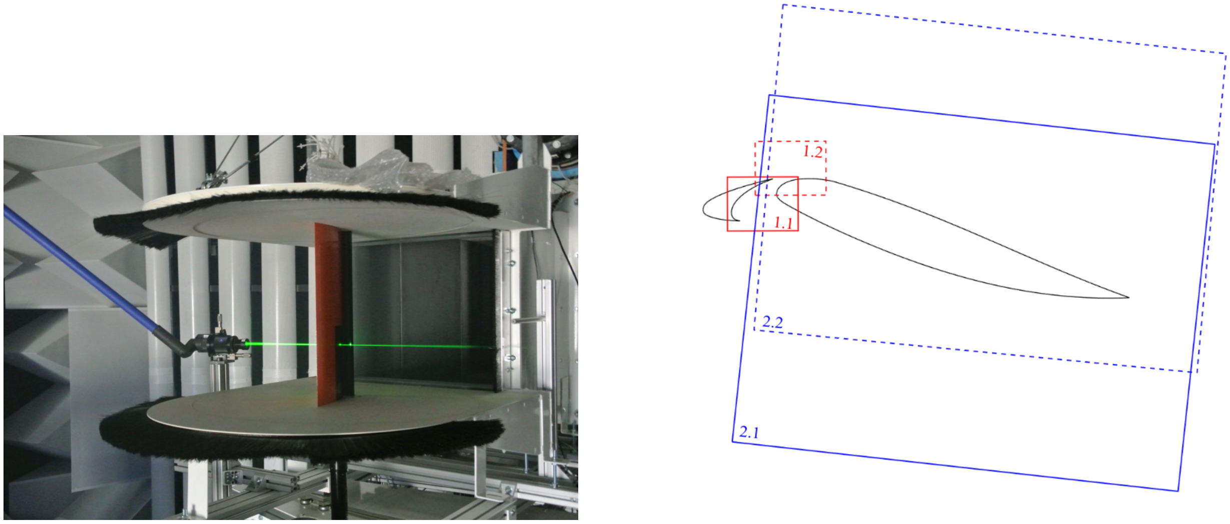

(a) PIV setup. **(b) Regions of interest selected for the PIV measurements.**

Fig. 5 Experimental setup and PIV acquisition regions

A. Pressure coefficient

Steady wall-pressure measurements were acquired using the same probes and acquisition channels employed for the unsteady pressure fluctuations. From these measurements, the pressure coefficient (C_p) distribution along the airfoil and slat surfaces was obtained.

Previously, the VALIANT project was conducted at the same test facility, featuring a smaller span of 300 mm and a larger chord length of 300 mm compared to the present test campaign. For the MAMBO campaign, the chord was reduced to 200 mm and the span was increased to 400 mm. The new nozzle outlet has a cross-section of 0.5 m in width and 0.4 m in height, whereas the previous VALIANT nozzle had a width of 0.4 m and a height of 0.3 m. In the latter case, the combination of a larger model and a smaller test section led to noticeable installation effects, which were expected to be mitigated in the present configuration by decreasing the chord and increasing the test-section area.

Fig. 6 presents a comparison between the two configurations, showing that the MAMBO airfoil exhibits lower C_p magnitudes across most of the surface. This trend is consistent with the anticipated reduction of wall-interference effects due to the improved blockage ratio of the current setup.

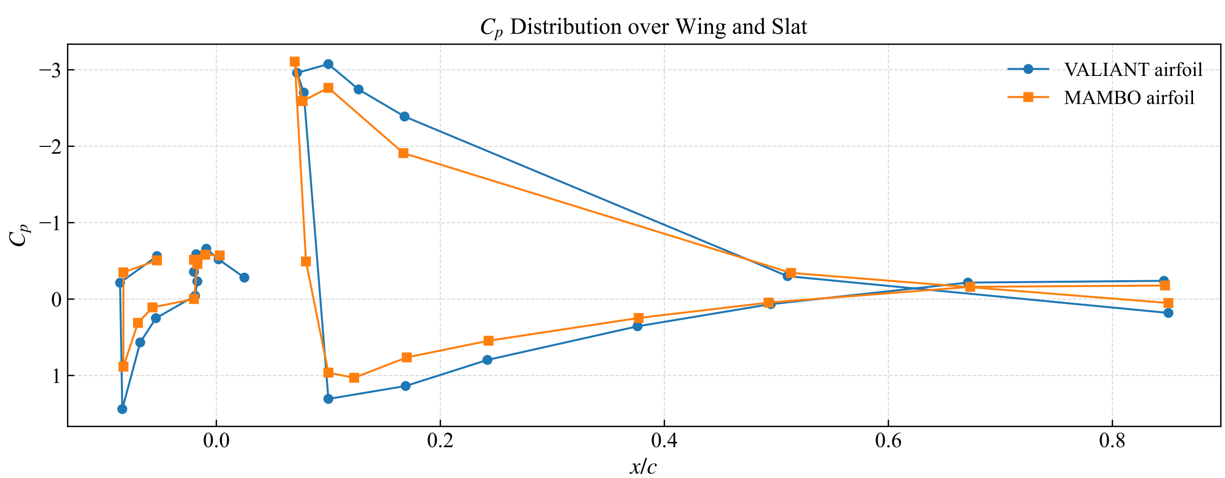

Fig. 6 Comparison between pressure coefficents (C_p) measured during the VALIANT and the MAMBO test campaigns

B. Acoustic spectral analysis

To analyze the radiated acoustic field, several microphones were employed. For clarity, the central microphone of the circular array (M4) is taken as reference. Fig. 7 presents the Power Spectral Density (PSD) for the three tested velocities, with measurements taken on both the extrados (G) and the intrados (D) sides of the profile. For each velocity, the spectra recorded on the intrados side are slightly higher in amplitude compared to those on the extrados. This can be explained by the orientation of the slat cove, which faces the intrados and therefore radiates more acoustic energy in that direction.

A clear dependency on flow speed is also observed. As the velocity increases from 25 to 75 $\mathrm{m\,s^{-1}}$, the overall sound levels rise, and the spectral peaks shift toward higher frequencies. In other words, higher flow speeds not only amplify the acoustic pressure but also generate tones at higher characteristic frequencies.

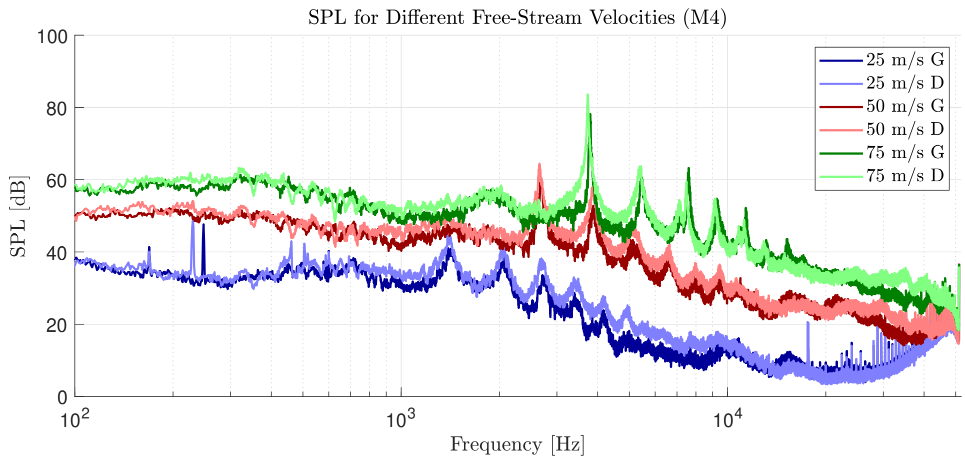

Fig. 7 Single-microphone spectra showing the effect of flow speed as a function of frequency

Regarding Fig. 8, the PSD is now expressed in terms of Strouhal number (Equation 1) in order to adimensionalize the results. Although the peaks for each velocity do not align perfectly, likely due to small uncertainties in the reference airspeed used for the scaling, a consistent range of $1.5 < St < 10$ is observed where the dominant tonal peaks appear. This range is in agreement with previous studies on slat noise [6].

$$St = \frac{f\,s}{U_\infty} \tag{1}$$

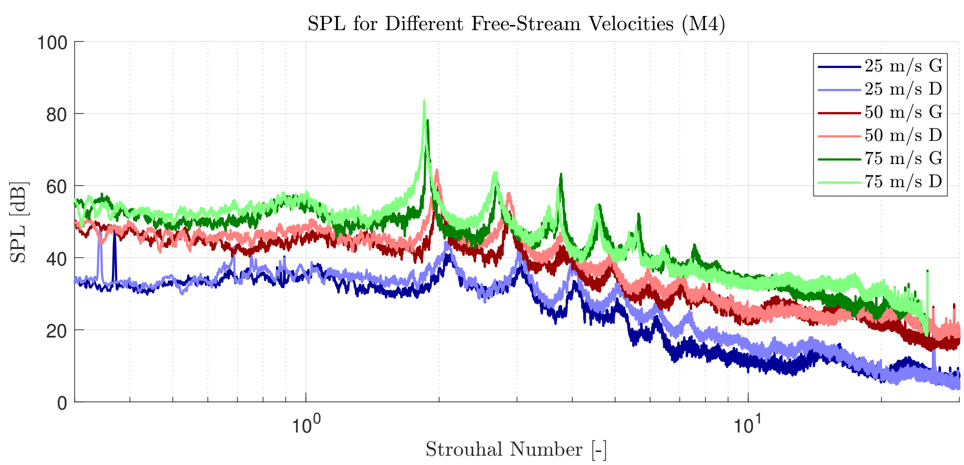

Fig. 8 Single-microphone spectra showing the effect of flow speed as a function of Strouhal number

This Strouhal range (and its corresponding frequency band) was then selected to compute the Overall Sound Pressure Level (OASPL) from the 60-second acoustic acquisition. The results, shown in Fig. 9, indicate an increase of approximately 13 dB between successive flow velocities, leading to an overall difference of about 26 dB between the lowest and highest speeds. In addition, the intrados consistently exhibits levels around 4 dB higher than the extrados.

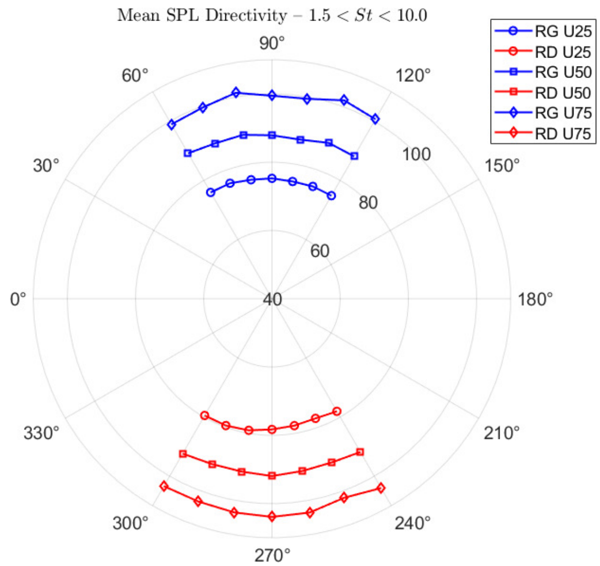

Fig. 9 OASPL Directivity

Fig. 10 shows the power spectral density (PSD) of the unsteady wall pressure signals measured at different locations along the airfoil surface for U_∞ = 50 m/s and a reference angle of 17.5°. The corresponding probe positions are indicated in Fig. 4.

A prominent observation is that the first spectral peak occurs at exactly the same frequency as the dominant peak in the far-field acoustic spectrum for the same flow condition (Fig. 7). This correspondence highlights the direct link between the wall pressure fluctuations and the radiated sound, emphasizing the role of flow dynamics in defining the acoustic signature of the wing-slat configuration. In particular, it suggests that the pressure fluctuations within the slat cavity and at its exit are key contributors to the broadband noise and tonal components observed in the acoustic measurements.

Furthermore, the relative amplitudes of the pressure spectra at the different probe locations provide insight into how the fluctuating flow structures interact with the airfoil surface. Higher energy levels near the cavity region (10b and 10f) are consistent with the intense vortex shedding and shear-layer instabilities identified in the PIV analysis, while the gradual decay of spectral energy further downstream (10a and 10d) indicates a loss of coherence as the structures are convected away. Moreover, Fig. 10a shows that probes located near the wing's leading edge—i.e., close to the cavity exit—are exposed to higher velocities and turbulence levels, which results in a significant amplification of the broadband content. In contrast, the probes positioned further downstream, towards the trailing edge, exhibit more pronounced tonal peaks, predominantly associated with the flow separation occurring over the suction side.

Together, these results underline the importance of coupling aerodynamic and acoustic measurements in order to fully characterize the noise generation mechanisms in such configurations.

C. PIV results

To ensure the quality of the flow incident on the model, hot-wire anemometry measurements were conducted at the outlet of the wind tunnel convergent before mounting the wing. Measurements were taken for all three velocities, and the ratio between the local velocity fluctuations and the mean velocity at each point was used to assess the turbulence level.

The highest values, around 2%, occur near the walls, whereas the central region, where the wing was mounted, exhibits significantly lower turbulence, approximately 0.4%. This analysis demonstrates that the flow approaching the wing is laminar enough to reliably reproduce realistic aerodynamic conditions, reducing experimental errors and improving the accuracy of the results.

The PIV data were processed in MATLAB to visualize the horizontal and vertical velocity components, its magnitude, the corresponding streamlines, and the vorticity field. Fig. 11a presents the time-averaged horizontal velocity (U)

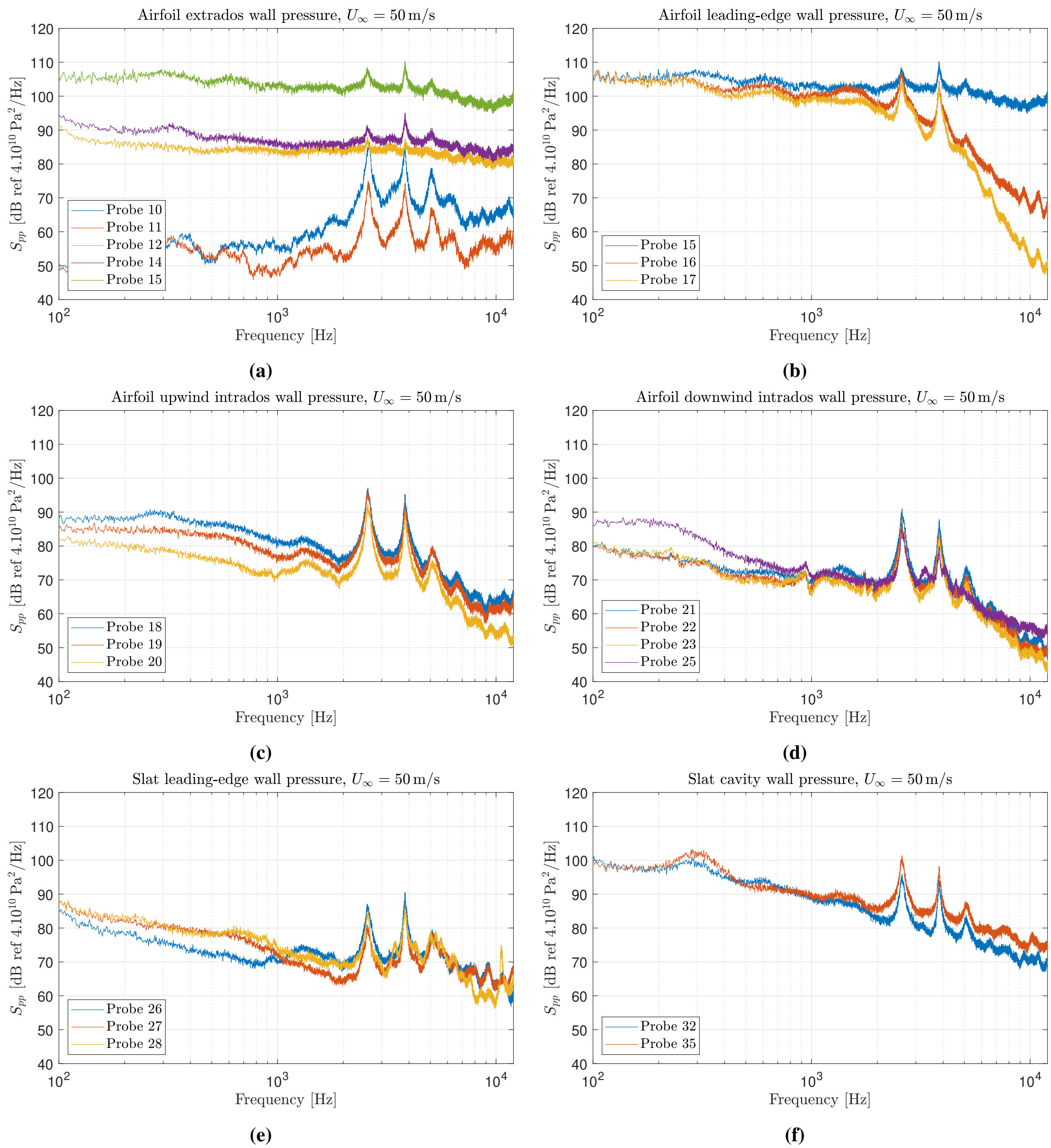

Fig. 10 Wall pressure spectra.

distribution obtained for the slat cove and its exit region. Similarly, Fig. 11b shows the time-averaged velocity magnitude ($|\mathbf{V}|$) for the same region, with streamlines superimposed. Figs. 12a and 12b display the vorticity field, including both the time-averaged and instantaneous results, respectively. All the figures mentioned correspond to the flow at $U_\infty = 50\,\mathrm{m\,s^{-1}}$, with the color scale normalized using the wing chord c as the characteristic length (for vorticity) and the free-stream velocity U_∞ as the reference speed.

The figures illustrate how fluid–structure interactions influence the velocity field throughout the flow domain. Near the leading edge of the main wing element, the velocity magnitude reaches up to 1.8 times the nominal free-stream velocity, indicating strong local acceleration over the extrados. This behavior is commonly associated with favorable

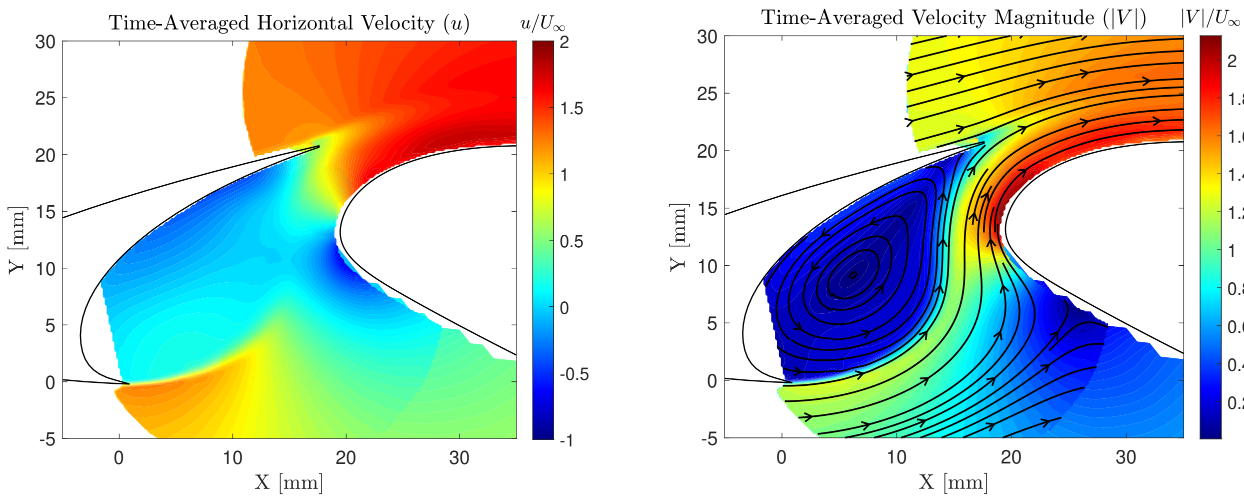

(a) U **component velocity field**

(b) |V| velocity magnitude field with streamlines

Fig. 11 Global view of the wing element from PIV data

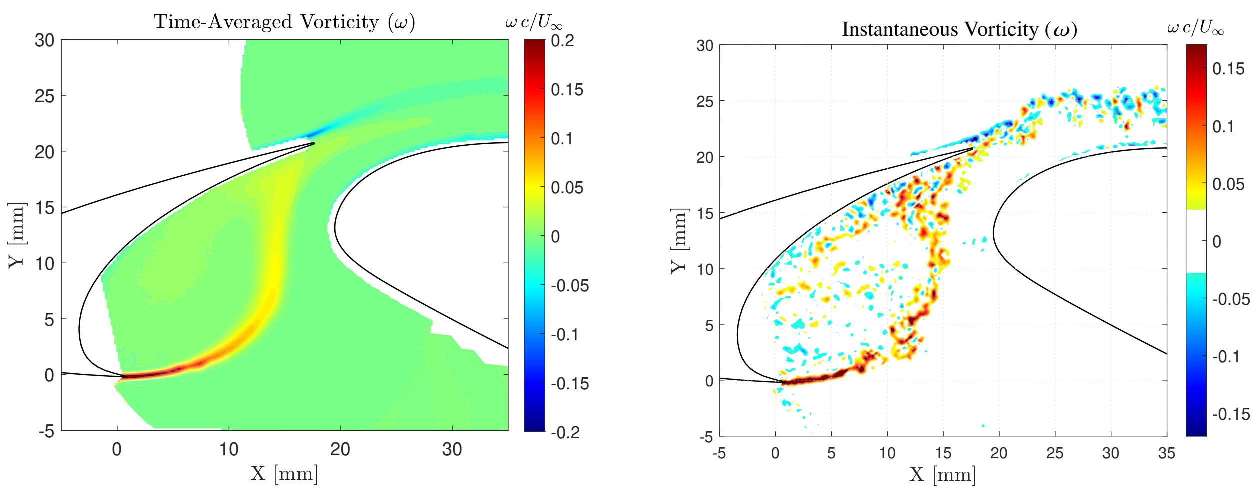

(a) Average vorticity field

(b) Instantaneous vorticity field

Fig. 12 Comparison between average and instantaneous vorticity fields measured by PIV

pressure gradients and surface curvature, which tend to guide and accelerate the flow along the airfoil surface.

In Fig. 11b, the streamlines expose a pronounced velocity discontinuity between the slat cove and the narrow passage adjacent to it. This abrupt variation indicates the presence of a shear layer, which becomes unstable as it convects downstream. The development of this instability promotes the formation of vortical structures, which are also highlighted in the time-averaged vorticity field shown in Fig. 12a. The spatial coherence of the vorticity path further supports the presence of organized unsteady flow in this region.

Inside the slat cove, the streamline pattern reveals a large recirculation zone, consistent with the typical flow separation observed in this region. As shown in prior studies, such as Zhang et al. [6], this recirculating flow originates near the lower slat surface and is bounded by a shear layer that may impinge on the main element, amplifying local velocity and pressure fluctuations. Depending on the instantaneous flow conditions, the shear-layer vortices may either be trapped within the cove or ejected through the slat gap, shaping the downstream flow behavior.

D. POD analysis

The Proper Orthogonal Decomposition (POD) is a method used to extract coherent structures from complex flows and to reduce the dimensionality of large datasets. It represents the flow field using an optimized orthonormal basis that captures the most energetic modes of the system. One efficient implementation of this technique is the snapshot method, which significantly reduces computational cost when the number of temporal samples is much smaller than the number of spatial points. This approach is widely used in fluid mechanics to analyze shear flows, vortex shedding, and boundary layers by separating the dominant spatial modes from their temporal evolution [17].

Fig. 13 presents the energy distribution across the first 200 POD modes. As expected, the first few modes capture the largest portion of the total kinetic energy, indicating their dominance in the flow dynamics. This energy decay provides insight into the coherence and complexity of the structures present in the flow. This energy profile can serve as a basis for selecting relevant modes in future velocity field reconstructions or targeted analyses, depending on the desired level of detail and accumulated energy.

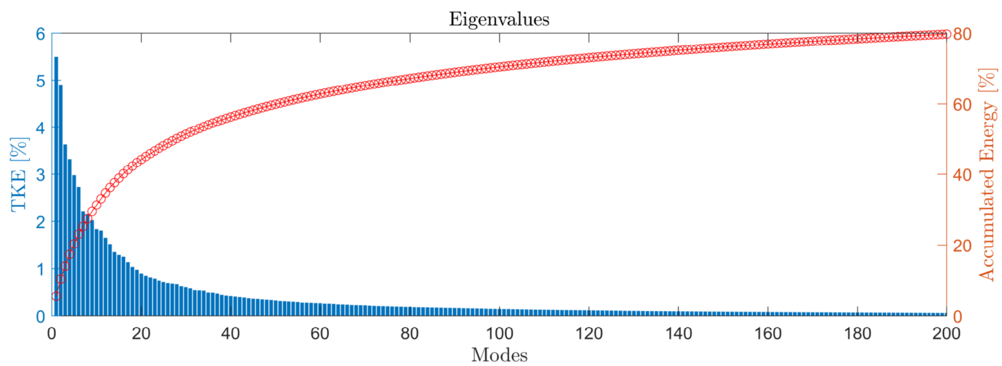

Fig. 13 Energy of POD Modes

At last, the spatial POD modes **U** represent flow patterns extracted from the data set. Each mode captures a part of a coherent structure that contributes significantly to the overall dynamics of the flow. These modes can be used for flow reconstruction, analysis of dominant behaviors, or model reduction in fluid simulations.

Fig. 14 presents POD Modes 1, 2, 4, 5, 8 and 10 (the 3rd mode was omitted as it closely resembles Mode 4 and would not contribute to additional structural insight). Modes 1, 2 and 5 highlight coherent structures that span both the recirculation zone within the slat cove and the shear layer downstream of the trailing edge, emphasizing their strong influence on the flow dynamics. In contrast, Modes 4, 8 and 10 tend to isolate these two regions, representing primarily the shear layer and the slat cove vortex, respectively. The streamlines were computed using both horizontal and vertical velocity components from spatial modes to provide a clearer visualization of the dominant flow patterns captured by each mode.

One of the major benefits of POD is the ability to reconstruct the flow field using only a selected set of spatial modes, filtering out noise and less relevant structures. However, defining the appropriate cutoff mode remains a challenge. To address this, a cross-correlation analysis between independent data sets representing the same flow configuration was performed. Inspired by the methodology presented in [18], this approach helps identify the mode up to which the flow structures remain consistent between datasets. Based on the correlation levels, the modes can be classified into highly correlated, moderately correlated, and uncorrelated, where the first two categories are likely to capture the dominant and meaningful features of the flow.

Fig. 16 presents the results of this analysis. The top panel shows the cross-correlation between two independent runs, while the bottom panel displays the maximum correlation coefficient for various pairs of runs, along with an averaged curve that serves as a basis for determining the cutoff modes. Spatial modes with a correlation above 80% were considered highly correlated and, therefore, representative of dominant structures. Conversely, correlation values below 60% were assumed to indicate uncorrelated modes, likely dominated by noise or non-recurrent features.

Table 2 summarizes the two cutoff thresholds identified for each side and free-stream velocity of the two detailed PIV zones (1.1 and 1.2). It can be observed that for the left side of the flow (zone 1.1), where the slat cavity is the main region of interest, the cutoff modes for both highly and moderately correlated structures remain essentially the same across the three tested velocities (25, 50, and 75 $\mathrm{m\,s^{-1}}$). This result highlights the robustness of the flow organization inside the cavity, showing that an increase in free-stream velocity does not lead to a significant loss of coherence or

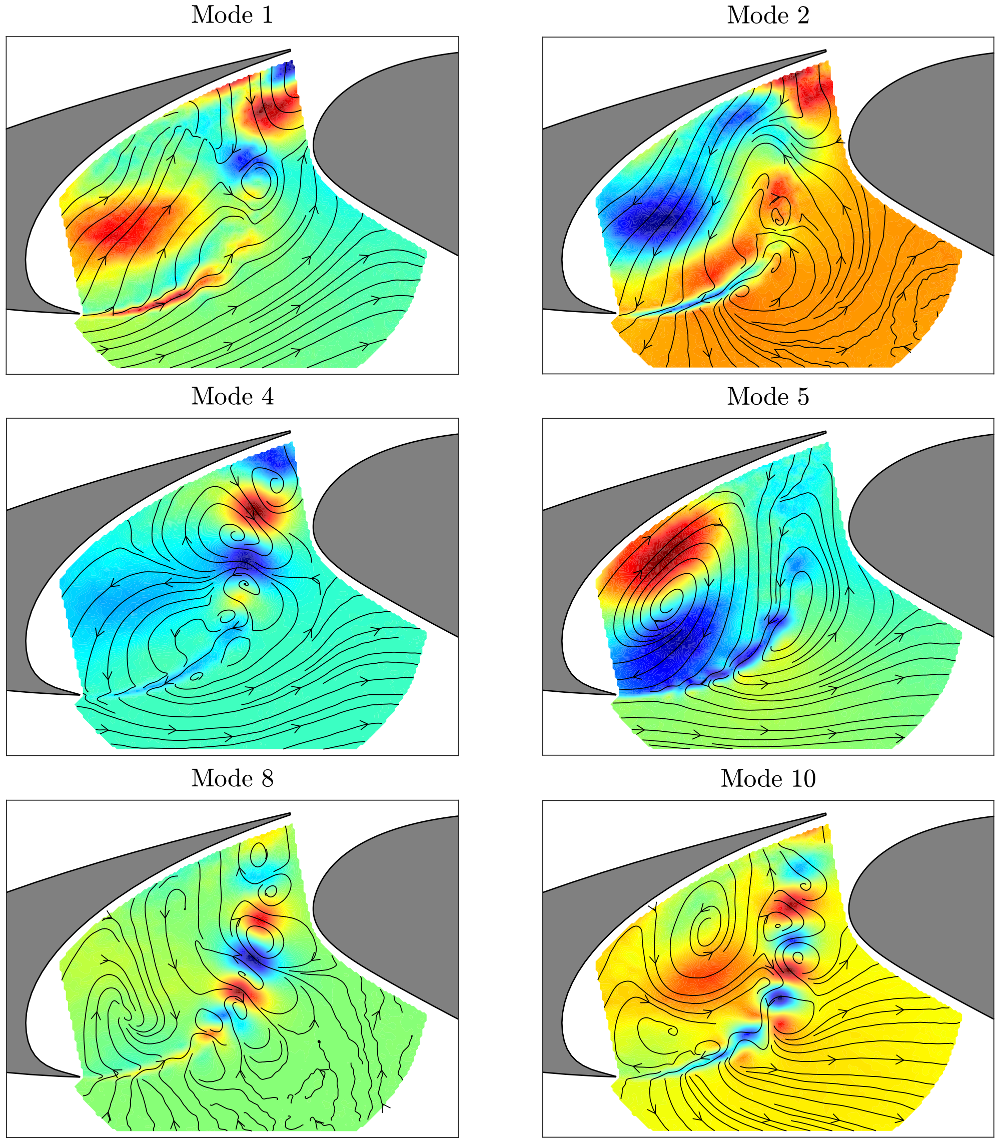

Fig. 14 Modes 1, 2, 4, 5, 8 and 10 of Horizontal Velocity Component at $25 m/s$

a premature cutoff of the POD modes. In other words, even at $75\,\mathrm{m\,s^{-1}}$, the flow retains a similar degree of spatial correlation as at lower velocities, suggesting that the rise in Reynolds number does not induce a noticeable degradation of modal consistency and that geometry-imposed dynamics outweigh velocity effects within the studied range.

This finding is further corroborated by the analysis of the shear layer, where the isolines of streamwise velocity display nearly identical shapes and trajectories for all three velocities. The persistence of this feature across conditions supports the interpretation that the dominant dynamics of the slat cavity flow are largely independent of the tested free-stream velocity. Consequently, the cutoff mode selection appears to be governed more by the intrinsic cavity dynamics than by external velocity variations. This consistency strengthens the validity of the chosen cutoff thresholds and provides confidence in the subsequent flow reconstructions.

For the extrados of the wing element, where the vortices ejected through the slat gap interact with the upper flow, different results are observed. The cutoff mode for the highly correlated case remains at low values, between 3 and 8, whereas for the moderately correlated case the value is roughly halved, around 24 for 25 and $75\,\mathrm{m\,s^{-1}}$ and 35 for $50\,\mathrm{m\,s^{-1}}$. Despite a slight difference at $50\,\mathrm{m\,s^{-1}}$, the cutoff modes for the three distinct velocities remain relatively consistent with one another, indicating good coherence and a certain Reynolds-number independence. Compared to zone 1.1, the decrease in values can be attributed to the stronger turbulence on this side of the flow, caused by the

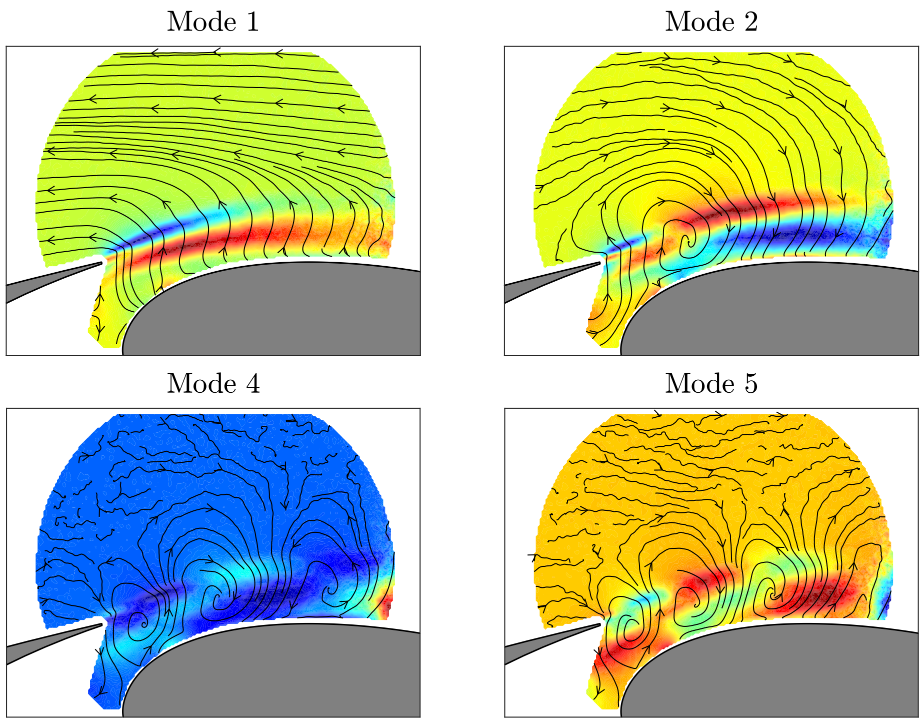

Fig. 15 Modes 1, 2, 4 and 5 of Vertical Velocity Component at $25m/s$

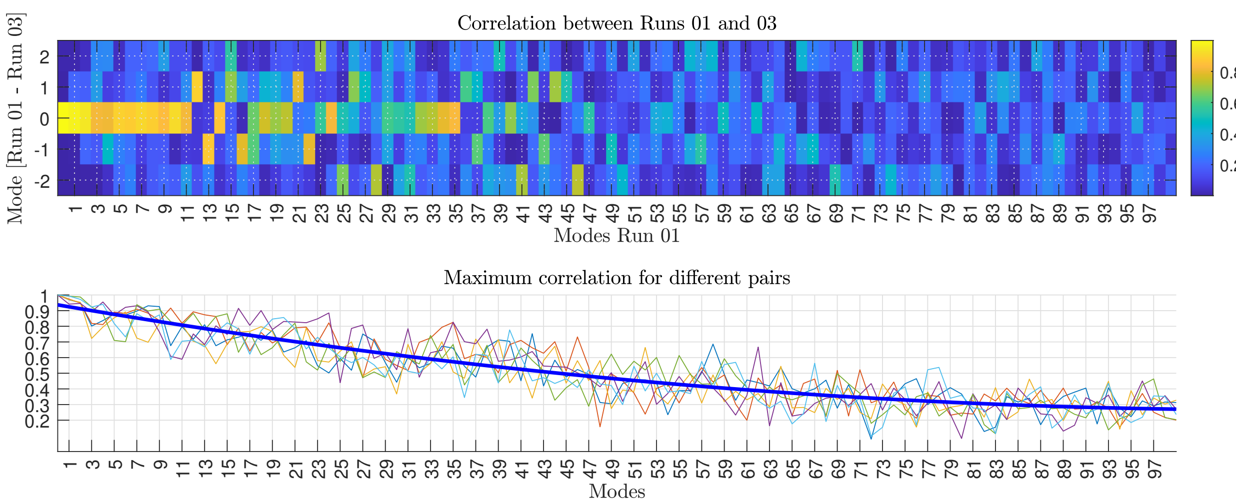

Fig. 16 Cross-Correlation of Pair of Runs

high-speed vortices interacting with the extrados flow, which reduces its predictability and coherence.

Zone	**U25**		**U50**		**U75**	
	k_{high}	k_{mod}	k_{high}	k_{mod}	k_{high}	k_{mod}
1.1	5	44	6	48	7	44
1.2	4	24	8	35	3	22

Table 2 Cutoff thresholds for highly and moderately correlated modes by side and free-stream velocity.

E. SPOD analysis

Advancing the analysis of coherent flow structures, another tool capable of identifying significant phenomena around the slat is the Spectral Proper Orthogonal Decomposition (SPOD). Its implementation, underlying logic, and computation closely resemble those of POD; however, instead of operating in the time domain, the dataset is analyzed in the frequency domain. This approach enables a more detailed examination and also allows validation of results obtained from other methods. In particular, the spatial and temporal coherence of SPOD modes facilitates their interpretation, as they can often be directly related to underlying flow mechanisms. The present study is based on the work of [19] and was carried out using the authors' MATLAB code adapted to Python.

To perform the SPOD analysis, it is necessary to define the target frequencies of interest, as SPOD provides a set of modes for each discretized frequency within the domain. In other words, for a selected frequency, SPOD returns modes ranked by energy from the most to the least energetic, according to their associated eigenvalues. Fig. 17 illustrates the energy spectrum of each mode across the frequency domain for PIV Zone 1.1 at $25\,\mathrm{m\,s^{-1}}$. It can be observed that the first mode is clearly dominant, as its amplitude is significantly higher than that of the second mode, indicating that it contains a substantial portion of the flow energy. A large separation between the eigenvalues associated with the first and the second SPOD modes is a good indicator for the dominance of one mechanism.

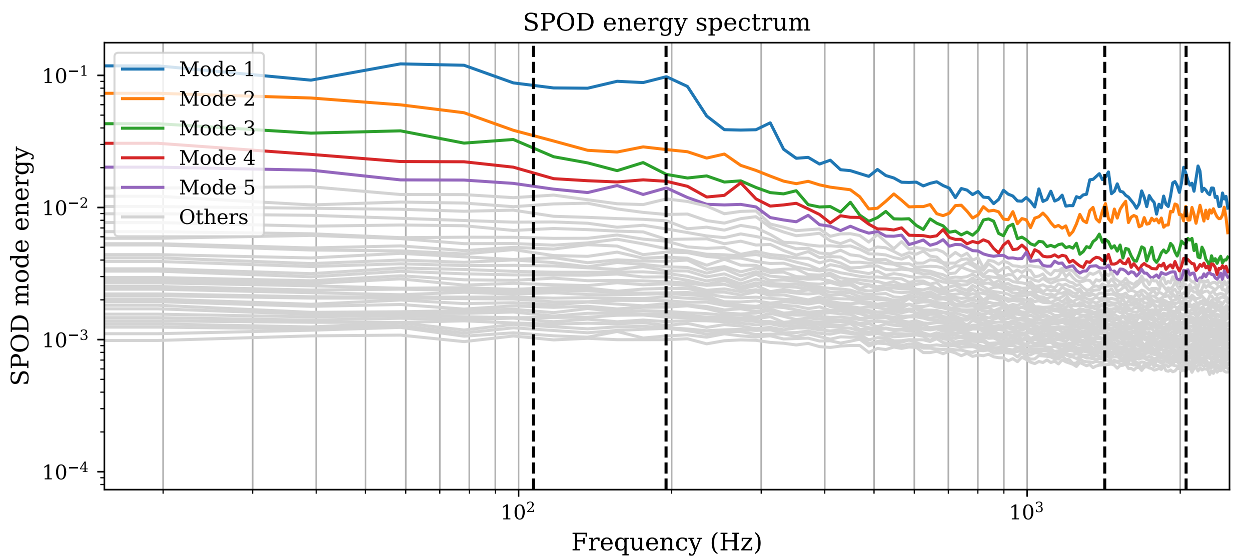

Fig. 17 Energetic distribution of SPOD modes at $U_\infty = 25\,\mathrm{m\,s^{-1}}$ for the U component of velocity

As previously stated, representative frequencies must be selected for the SPOD analysis. From the acoustic spectrum shown in Fig. 7, the first two peaks at $25\,\mathrm{m\,s^{-1}}$ occur at 1421 Hz and 2054 Hz. Additionally, the frequency of 107 Hz was selected based on the definition of $St = 0.16$ for the slat cove recirculation flow provided in [20, 21]. The spectral content is computed using FFT blocks of 256 samples, corresponding to a Hanning window of 0.0512 s (for a sampling frequency of 5 kHz), resulting in a frequency resolution of 19.53 Hz.

Fig. 18 presents the first three modes corresponding to the selected frequencies. It should be noted that the value indicated in the title corresponds to the closest discretized frequency to the target value. For the first mode at 117 Hz, the spatial distribution clearly corresponds to the slat cove flow, which is also prominent in POD Mode 5 (Fig. 14). This observation is consistent with the correspondence between lower-energy POD modes and low-frequency, low-order SPOD modes, which are associated with the recirculating flow inside the slat cove. For the frequencies associated with the tonal peaks in the acoustic spectrum (1426 Hz and 2051 Hz), the spatial modes exhibit a clear relation to the formation, ejection, and convection of vortical structures generated at the slat trailing edge. These modes highlight coherent patterns aligned with the shear layer dynamics, reinforcing the connection between the flow structures identified through SPOD and the acoustic signatures observed in the spectrum. The presence of the 800 Hz modes will be discussed at the end of this section.

The second mode also exhibits coherence with the dominant flow structures, suggesting that it still retains enough energy to capture some of the main features of the dynamics under investigation. Its spatial organization remains

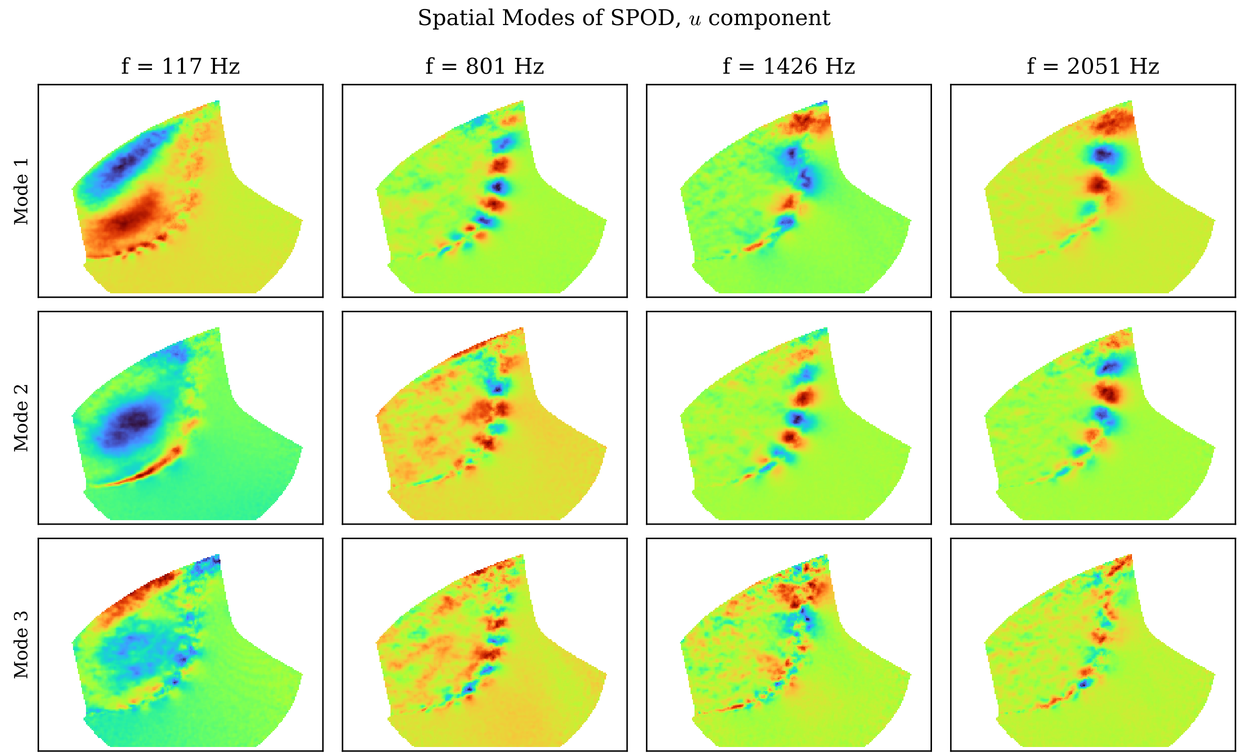

Fig. 18 First 3 modes at four representative frequencies at $U_\infty = 25\,\mathrm{m\,s^{-1}}$

identifiable, with patterns that can be related to those observed in the most energetic mode. In contrast, the third mode shows a noticeable degradation in coherence, with a more irregular and fragmented spatial distribution. This behavior suggests a lower energetic contribution, making it more challenging to identify and isolate underlying coherent structures, as they become increasingly obscured by less organized fluctuations.

Interestingly, by plotting the first mode at each frequency, it can be observed that the vortex shedding structures do not appear exclusively at the first peak frequency. In fact, similar patterns to those identified in the POD modes, as well as at 1426 Hz and 2051 Hz, are already discernible around 800 Hz. This indicates that the presence of vortical structures alone is not necessarily associated with significant acoustic radiation, as no notable variation is observed in the acoustic spectrum at this frequency.

Another relevant observation arises from applying the same procedure to the case with $U_\infty = 50\,\mathrm{m\,s^{-1}}$. In this condition, the vortex shedding pattern becomes barely distinguishable. As indicated in Fig. 7, the tonal noise peaks shift to frequencies beyond the 2500 Hz limitation imposed by the PIV sampling. These results further support the relation between slat tonal noise and the processes of vortex ejection and impact within the shear layer. In this sense, the interpretation of SPOD results benefits from considering both the modal structures and their associated spectral content, as the latter provides context regarding the relative importance of each mode.

F. Vortex identification

After determining the cutoff modes, the flow field is reconstructed, allowing the separation and analysis of two distinct components: the highly correlated and the moderately correlated portions. For the slat cove region at $U_\infty = 25\,\mathrm{m\,s^{-1}}$, the first component primarily captures the large-scale recirculating motion within the cavity, while the second is clearly dominated by small-scale turbulent vortices generated at the slat's trailing edge. This analysis provides the foundation for this next part of the study.

As mentioned before, a good portion of the noise generated by a wing equipped with a leading-edge slat originates from the formation of both large and small-scale vortices. These structures impinge upon solid surfaces, causing pressure fluctuations that contribute to acoustic emissions. One of the key challenges in this analysis is to determine the path taken by these vortices, as they can either be trapped inside the slat cove by recirculation or ejected through the slat gap and impact the main wing surface.

Vorticity is a key concept for analyzing turbulent flows. Several criteria have been proposed to identify and quantify vortical structures, such as the Q and λ_2 criteria. More recently, the Γ_1 and Γ_2 functions have been successfully applied due to their simplicity and clarity in representing vortical regions [22]. The Γ_1 function is defined using velocity vectors located within a neighborhood S around a point of interest P. The size of this window affects the sensitivity of the analysis and consists of N discrete points M_i corresponding to the centers of the grid cells. The function computes a weighted average of the cross product between the position vector $\overline{PM}$ and the velocity vector $\mathbf{U_M}$ at point M,

$$\Gamma_1(P) = \frac{1}{S}\int_S \sin(\theta_M) = \frac{1}{N}\sum \sin(\theta_M) \tag{2}$$

where, θ_M is the angle between the vectors $\overline{PM}$ and $\mathbf{U_M}$, as depicted in Fig. 19. The Γ_1 function yields normalized values between -1 and +1, indicating the likelihood that point P is the center of a vortex.

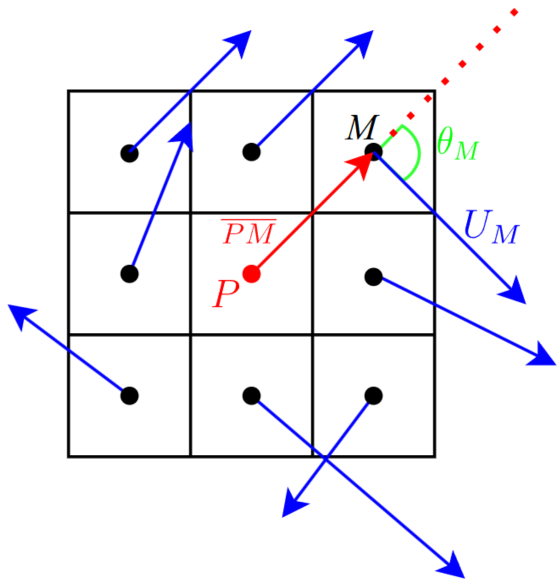

Fig. 19 Scheme of the Γ_1 function variables

The Γ_2 function follows a similar principle but subtracts the spatial mean velocity inside the window S from each velocity vector before computation. This adjustment makes Γ_2 Galilean invariant, meaning the analysis becomes independent of the global motion of the flow. Moreover, a threshold for Γ_2 ($|\Gamma_2| > \frac{\pi}{2}$) can be established to detect regions where rotation is dominant over shear or stretching, allowing estimation of vortex radius. In the following figures, the black contour highlights the areas where this threshold is satisfied and rotational effects prevail. Further analysis of critical points such as nodes and saddle points is explored by Depardon et al. [23], helping to interpret local flow topology.

The method presented above was applied to the PIV velocity fields in an attempt to track the path of the formed vortices. However, due to the large amount of data and the turbulent nature of the flow, the results were too noisy to accurately identify vortex centers (see Fig. 20). Therefore, the algorithm was instead implemented on the reconstructed velocity fields obtained via POD, separately for each part of the correlated motions. This approach yielded significantly more promising results.

For the first group of POD modes, the highest values of the Γ_1 function were concentrated in the center of the cavity, highlighting the presence of a recirculating flow inside the slat cove. The vortex center was not completely stationary, as spanwise motions caused slight displacements within the cavity. Fig. 21a illustrates a representative instant of the reconstructed flow.

As for the moderately correlated POD modes (Fig. 21b, the results proved even more insightful. Since these modes predominantly capture the vortices shed from the slat's trailing edge and formed within the shear layer, each time step

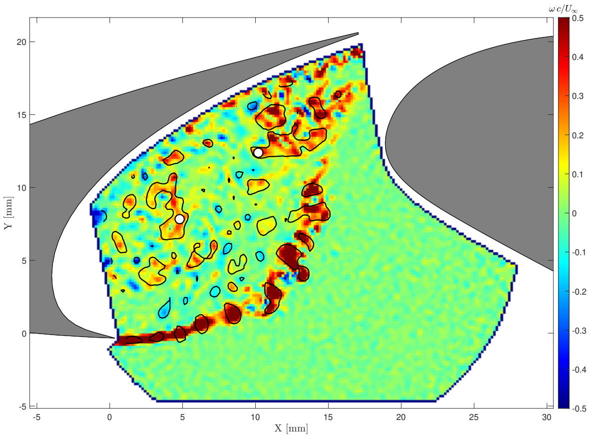

Fig. 20 Γ_1 applied to original PIV flow

revealed multiple potential vortex centers. Notably, the results align with existing insights from slat aerodynamics: such vortices may either be recaptured by the cavity's recirculation or ejected through the slat gap, where the velocity magnitude peaks. These two distinct trajectories are closely linked to noise generation mechanisms and are crucial to understanding the aeroacoustic behavior of the configuration. (∘) represents counterclockwise rotation while (**×**) indicate clockwise rotation.

To investigate whether the trajectories of these vortices depend on the free-stream velocity, the coordinates of the identified structures were stored at every time instant and then a polynomial interpolation was applied to obtain an average trajectory. The results are presented, for all three velocities, in Fig. 22, where the gray lines represent the instantaneous vortex path obtained, while the red line depicts the average trajectory over the selected time interval.

It can be observed that, despite the increase in free-stream velocity, the average trajectories of the ejected vortices remain essentially unchanged. This suggests that the convection path of the vortical structures is weakly dependent on the Reynolds number within the tested range. Moreover, the identified trajectory coincides with the shear layer visible in Fig. 11b and with the mean vorticity distribution in Fig. 12a, reinforcing the consistency between the instantaneous dynamics and the time-averaged flow features.

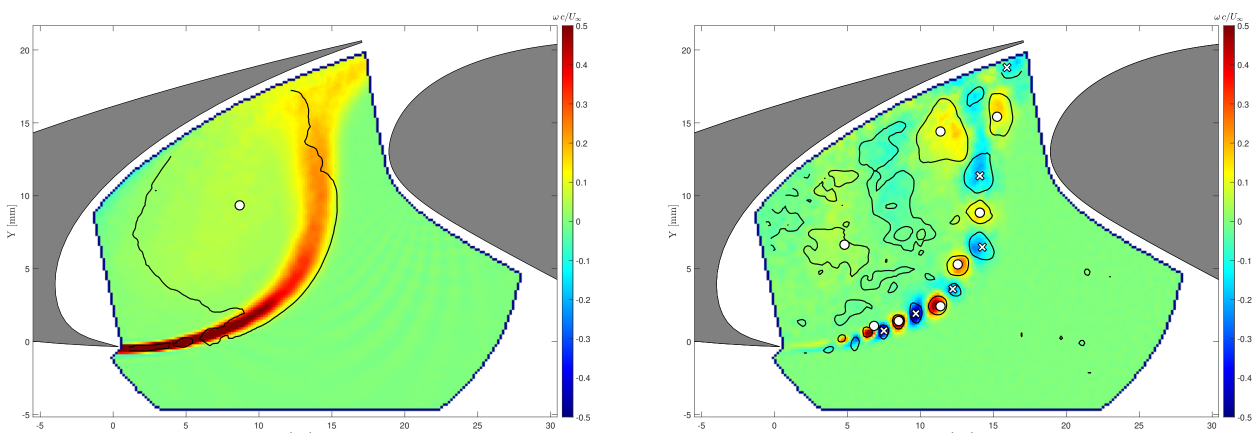

(a) Highly correlated modes **(b) Moderately correlated modes**

Fig. 21 Comparison of Γ_1 for different flow regimes

G. Cross-Correlation

Cross-correlation was initially proposed as a statistical tool to quantify the degree of similarity between two signals as a function of a temporal or spatial shift. In turbulent flow analysis, it allows the investigation of coherence between

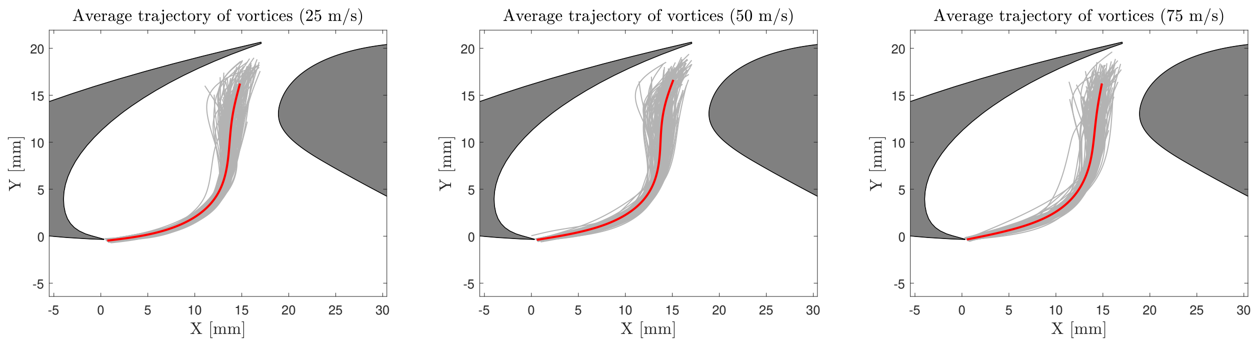

(a) 25 m s^{-1} **(b)** 50 m s^{-1} **(c)** 75 m s^{-1}

Fig. 22 Trajectory of vortices at different flow speeds

spatial structures at different locations or between temporal signals acquired at distinct measurement points [24].

To account for potential time delays between signals, the correlation function introduces a temporal shift variable, enabling the identification of the precise delay at which maximum correlation occurs. The cross-correlation function $S_{\phi' p'}$ is computed between the fluctuations of the velocity fields U and V—collectively denoted as ϕ—obtained from PIV, and the pressure fluctuations p from microphone data. It is defined as,

$$S_{\phi' p'}(\mathbf{x}, \mathbf{y}, \tau) = \frac{1}{N} \sum_{n=1}^{N} [\phi'(\mathbf{x}, t_n) p'(\mathbf{y}, t_n + \tau)], \tag{3}$$

where $\mathbf{x}$ and t_n represent the spatial and temporal indices of the velocity measurements, $\mathbf{y}$ is the microphone position, τ is the time shift, and N is the number of PIV samples.

A normalized correlation coefficient $R_{\phi' p'}$ can also be computed using the standard deviations $\sigma_{\phi'}(\mathbf{x})$ and $\sigma_{p'}$ of the respective signals, as shown in Equation 4. Note that for PIV data, each spatial point has a distinct $\sigma_{\phi'}$, while $\sigma_{p'}$ remains constant for each microphone.

$$R_{\phi' p'}(\mathbf{x}, \mathbf{y}, \tau) = \frac{S_{\phi' p'}(\mathbf{x}, \mathbf{y}, \tau)}{\sigma_{\phi'}(\mathbf{x})\, \sigma_{p'}} \tag{4}$$

The time shift τ corresponding to the maximum of $R_{\phi' p'}$ indicates the delay at which the two signals are most correlated.

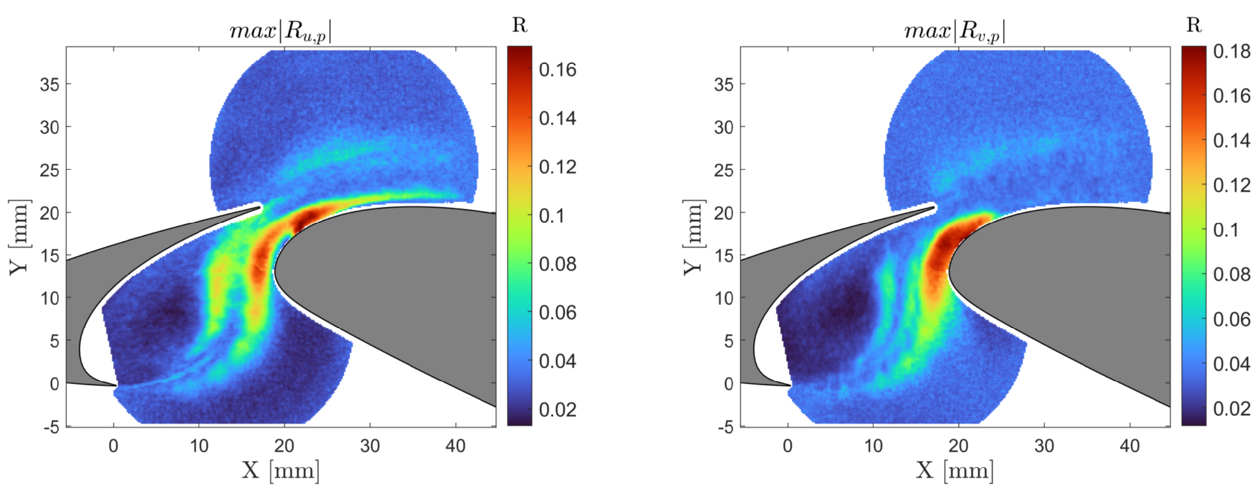

(a) *u* **component** **(b)** *v* **component**

Fig. 23 Cross-correlation coefficient ***R*** **maps between PIV velocity fields and acoustic signature**

The cross-correlation technique was applied between the PIV velocity fields (both U and V components) and the pressure signals measured by the circular microphone array. Since PIV data was acquired at 5 kHz and the acoustic data at 102.4 kHz, the acoustic signal was downsampled to 5 kHz to match the temporal resolution of the PIV measurements. This step ensured compatibility between the datasets without introducing artificial information through interpolation. The algorithm was then executed to compute the normalized cross-correlation coefficient R for each point in the PIV domain, highlighting the regions most correlated with noise generation.

This calculation was performed for five independent runs, and the resulting maps were averaged to improve statistical reliability, as presented in Fig. 23a. It is particularly evident, especially for the vertical velocity component V, that regions near the leading edge of the main element and the cavity exit exhibit strong correlation with the measured acoustic pressure. Additionally, the horizontal component U reveals that the flow along the shear layer contributes significantly to the radiated noise, likely due to the vortex displacement in that region, which tends to follow distinct paths.

As a reminder, each side of the flow was acquired independently, at different times. The high coherence observed between the left and right sides highlights the reliability of both the measurements and the cross-correlation analysis.

V. Conclusion

Based on the analysis of the available PIV data, this study has provided important insights into the aerodynamic phenomena occurring around the slat and their connection to noise generation. The measurements revealed the presence of a large recirculation zone within the cove, bounded by an unstable shear layer that promotes the formation of vortical structures. The application of POD enabled the separation of the flow dynamics into highly correlated and moderately correlated components, thereby isolating large-scale recirculating motion from smaller-scale vortices shed from the trailing edge. This decomposition not only clarified the spatial organization of the flow but also allowed the application of vortex-identification algorithms, leading to a more precise characterization of the underlying mechanisms, which were further supported by the SPOD analysis.

The correlation analysis further demonstrated that vortices, particularly those convected along the shear layer and intermittently ejected from the cavity, are strongly linked to acoustic pressure fluctuations. Regions near the leading edge and cavity exit were identified as dominant contributors to broadband noise, while the flow closer to the trailing edge displayed more distinct tonal features associated with vortex shedding. Overall, the results provide a coherent picture of how the complex slat-cove dynamics influence the aeroacoustic behavior of the configuration and establish a foundation for future investigations and potential noise-reduction strategies.

Acknowledgments

The present work is part of the program MAMBO "Méthodes avancées pour la modélisation du bruit moteur et avion" (Advanced Methods for Engine and Aicraft Noise Modelling) coordinated by Airbus SAS. It was supported by the Direction Générale de l'Aviation Civile (DGAC) under the Grant n° 2021-50. This study was financed in part by the Coordenação de Aperfeiçoamento de Pessoal de Nível Superior - Brasil (CAPES) – Finance Code 001. The authors kindly acknowledge Pierre Duquesne for fruitful discussions and guidance on the POD analysis, as well as Jean-Charles Vingiano and Pascal Souchotte for support during the experimental campaign, and Guilherme Henrique Pick Costa for providing the SPOD code used in this work. In addition, the authors acknowledge Florian Guiho (Airbus) for valuable exchanges regarding the geometry and data.

References

[1] Powell, C. A., and Fields, J. M., "Human Response to Aircraft Noise," Tech. Rep. NASA-CR-187553, NASA, 1992.

[2] ICAO, I. C. A. O., "Environmental Report 2016: Aircraft Noise – Chapter 2," , 2016. URL `https://www.icao.int/environmental-protection/Pages/env2016.aspx`.

[3] Filippone, A., "Aircraft Noise Prediction," *Progress in Aerospace Sciences*, Vol. 68, 2014, pp. 27–63. https://doi.org/10.1016/j.paerosci.2014.02.001.

[4] Anderson, J. D., *Fundamentals of Aerodynamics*, 4th ed., McGraw-Hill, New York, 2007.

[5] Yu, Y., and Zorumski, W. E., "A Review of Airframe Noise Research: Successes, Challenges, and Future Directions," *Progress in Aerospace Sciences*, Vol. 33, No. 12, 1997, pp. 655–687. https://doi.org/10.1016/S0376-0421(97)00006-7.

[6] Zhang, Y., Cattafesta, L., Pascioni, K., and Choudhari, M., "Slat Noise in High-Lift Systems," *Progress in Aerospace Sciences*, Vol. 125, 2021, p. 100717. https://doi.org/10.1016/j.paerosci.2021.100717.

[7] Guo, Y., "An Aeroacoustic Study of a Leading Edge Slat Configuration," *International Journal of Aeroacoustics*, Vol. 1, No. 3, 2002, pp. 241–274. https://doi.org/10.1260/147547202320962583.

[8] Dam, C., "The Aerodynamic Design of Multi-Element High-Lift Systems for Transport Airplanes," *Progress in Aerospace Sciences*, Vol. 38, 2002, pp. 101–144. https://doi.org/10.1016/S0376-0421(02)00002-7.

[9] Takeda, K., Ashcroft, G. B., Zhang, X., and Nelson, P. A., "Unsteady Aerodynamics of Slat Cove Flow in a High-Lift Device Configuration," *39th Aerospace Sciences Meeting and Exhibit*, Reno, NV, 2001. https://doi.org/10.2514/6.2001-0706.

[10] Pascioni, K. A., and Cattafesta, L. N., "An Aeroacoustic Study of a Leading-Edge Slat: Beamforming and Far Field Estimation Using Near Field Quantities," *Journal of Sound and Vibration*, Vol. 429, 2018, pp. 224–244. https://doi.org/10.1016/j.jsv.2018.05.029.

[11] Terracol, M., Manoha, E., and Lemoine, B., "Investigation of the Unsteady Flow and Noise Generation in a Slat Cove," *AIAA Journal*, Vol. 54, No. 2, 2016, pp. 469–489. https://doi.org/10.2514/1.J053479.

[12] Henning, A., Wrede, B., and Geisler, R., "Aeroacoustic Investigation of a High-Lift Device by Means of Synchronized PIV and Microphone Measurements," *Proceedings of the 16th International Symposium on Applications of Laser Techniques to Fluid Mechanics*, Lisbon, 2012.

[13] Mironov, M. A., Belyaev, I. V., Kopiev, V., and Sorokin, A. A., "An Experimental Study of Reducing Narrowband Noise of a Slat Using Chevrons," *Acoustical Physics*, Vol. 58, No. 4, 2012, pp. 435–443. https://doi.org/10.1134/S1063771012040161.

[14] Wild, J., Pott-Pollenske, M., and Nagel, B., "An Integrated Design Approach for Low-Noise High-Lift Devices," *Proceedings of the 3rd AIAA Flow Control Conference*, AIAA, San Francisco, CA, 2006. https://doi.org/10.2514/6.2006-2843.

[15] Leclère, Q., Pereira, A., Finez, A., and Souchotte, P., "Indirect Calibration of a Large Microphone Array for In-Duct Acoustic Measurements," *Journal of Sound and Vibration*, Vol. 376, 2016, pp. 48–59. https://doi.org/10.1016/j.jsv.2016.04.033.

[16] Raffel, M., Willert, C. E., Wereley, S. T., and Kompenhans, J., *Particle Image Velocimetry: A Practical Guide*, 2nd ed., Springer, Berlin, 2007. https://doi.org/10.1007/978-3-540-72308-0.

[17] Sirovich, L., "Turbulence and the Dynamics of Coherent Structures. I. Coherent Structures," *Quarterly of Applied Mathematics*, Vol. 45, No. 3, 1987, pp. 561–571.

[18] Butcher, D., and Spencer, A., "Cross-Correlation of POD Spatial Modes for the Separation of Stochastic Turbulence and Coherent Structures," *Fluids*, Vol. 4, No. 3, 2019, p. 134. https://doi.org/10.3390/fluids4030134.

[19] Schmidt, O. T., and Colonius, T., "Guide to Spectral Proper Orthogonal Decomposition," *AIAA Journal*, Vol. 58, No. 3, 2020. https://doi.org/10.2514/1.J058809.

[20] Murali, A. R., "Dynamics, Mechanisms, and Surrogate Modelling of Noise from a Leading Edge Slat," Ph.D. thesis, Université de Lyon, École Centrale de Lyon, Lyon, France, 2025.

[21] Murali, A. R., Boudet, J., Jacob, M. C., Guihot, F., Bauerheim, M., and Moreau, S., "Noise Radiation and Dynamics of Slat Cove Vortices Revisited in Light of a Parametric LBM Study," *30th AIAA/CEAS Aeroacoustics Conference*, Rome, Italy, 2024, pp. AIAA Paper 2024–3348. https://doi.org/10.2514/6.2024-3348.

[22] Graftieaux, L., Michard, M., and Grosjean, N., "Combining PIV, POD and Vortex Identification Algorithms for the Study of Unsteady Turbulent Swirling Flows," *Measurement Science and Technology*, Vol. 12, No. 9, 2001, pp. 1422–1429. https://doi.org/10.1088/0957-0233/12/9/307.

[23] Depardon, S., Vassilicos, J. C., and Lévêque, E., "Instantaneous Skin-Friction Pattern Analysis Using Automated Critical Point Detection on Near-Wall PIV Data," *Measurement Science and Technology*, Vol. 17, No. 5, 2006, pp. 969–976. https://doi.org/10.1088/0957-0233/17/5/019.

[24] Rackl, R., and Siddon, T. E., "Causality Correlation Analysis of Flow Noise with Fluid Dilatation as Source Fluctuation," *Journal of the Acoustical Society of America*, Vol. 65, No. 5, 1979, pp. 1147–1155.